

# Can we explain non-typical solar flares?

K. Dalmasse,<sup>1</sup> R. Chandra,<sup>2</sup> B. Schmieder,<sup>1</sup> and G. Aulanier<sup>1</sup>

<sup>1</sup> LESIA, Observatoire de Paris, LESIA, CNRS, UPMC, Univ. Paris Diderot, 5 place Jules Janseen, 92190 Meudon, France

<sup>2</sup> Department of Physics, DSB Campus, Kumaun University, Nainital- 263 002, India

## ABSTRACT

**Context.** We used multi-wavelength high-resolution data from ARIES, THEMIS, and SDO instruments, to analyze a non-standard, C3.3 class flare produced within the active region NOAA 11589 on 2012 October 16. Magnetic flux emergence and cancellation were continuously detected within the active region, the latter leading to the formation of two filaments.

**Aims.** Our aim is to identify the origins of the flare taking into account the complex dynamics of its close surroundings.

**Methods.** We analyzed the magnetic topology of the active region using a linear force-free field extrapolation to derive its 3D magnetic configuration and the location of quasi-separatrix layers (QSLs) which are preferential sites for flaring activity. Because the active region's magnetic field was nonlinear force-free, we completed a parametric study using different linear force-free field extrapolations to demonstrate the robustness of the derived QSLs.

**Results.** The topological analysis shows that the active region presented a complex magnetic configuration comprising several QSLs. The considered data set suggests that an emerging flux episode played a key role for triggering the flare. The emerging flux likely activated the complex system of QSLs leading to multiple coronal magnetic reconnections within the QSLs. This scenario accounts for the observed signatures: the two extended flare-ribbons developed at locations matched by the photospheric footprints of the QSLs, and were accompanied with flare loops that formed *above* the two filaments which played no important role in the flare dynamics.

**Conclusions.** This is a typical example of a complex flare that can a-priori show standard flare signatures that are nevertheless impossible to interpret with any standard model of eruptive or confined flare. We find that a topological analysis however permitted to unveil the development of such complex sets of flare signatures.

**Key words.** Sun: flares / Sun: corona / Sun: filaments, prominences / Sun: magnetic fields / magnetic reconnection

## 1. Introduction

Solar flares are the most energetic events on the sun. They emit radiation over the whole electromagnetic spectrum from  $\gamma$ -rays to radio wavelengths (Shibata 1999; Shibata & Magara 2011). Magnetic reconnection is the main process that releases energy during the solar flares. This energy is extracted from the magnetic energy that is stored in current-carrying fields in the corona. During a flare, energetic particles and thermal energy are produced around the reconnection site. They flow down towards the lower and denser layers of the solar atmosphere. As a result, coronal emission is produced within and around (post) flare loops, and surface brightenings occur along so-called flare ribbons, as observed in the ultraviolet (UV) as well as in typically-chromospheric wavelengths such as  $H\alpha$ . Solar flares are usually classified into two categories: eruptive or confined.

When a flare is associated with a coronal mass ejection (CMEs), either being associated with a detectable filament eruption or not, it is an eruptive flare. Those are often referred to as two-ribbon flares and long duration events, because they are associated with two parallel flare ribbons, that are located on both sides of the polarity inversion line (PIL), and that gradually move apart from one another. So as to explain the different observational manifestations of eruptive flares such as filament eruptions when they are observed, ribbon separations, flare loops formation, and associated phenomena, the standard CSHKP flare model was developed in two dimensions (Carmichael 1964; Sturrock 1966; Hirayama 1974; Kopp & Pneuman 1976; Forbes & Malherbe 1986). According

to this model, a current sheet forms in the corona, right below the erupting filament. Magnetic field lines sequentially reconnect at this current sheet, resulting in a growing (resp. spreading) system of flare loops (resp. ribbons), located below the erupting filament. Some 3D extensions to this model have been recently proposed to explain observational properties and physical processes, firstly in the form of cartoons (Shibata et al. 1995; Moore et al. 2001; Priest & Forbes 2002) and more recently based on numerical simulations (Aulanier et al. 2012; Kusano et al. 2012; Janvier et al. 2013).

The other flares, that are not associated with a CME, are the confined flares. Those are classically due to loop-loop interactions in the corona, which are induced by horizontal motions or flux emergence through the photosphere (*e.g.*, Gorbachev & Somov 1989; Démoulin et al. 1997; Hanaoka 1997; Mandrini et al. 1997; Schmieder et al. 1997; Nishio et al. 1997; Chandra et al. 2006). Confined flares are usually associated with multiple ribbons. The classical two-dimensional picture for the magnetic configuration and reconnection behavior in such flares is that of a coronal X-point, at which a current sheet is gradually formed as a result of the photospheric motions (Giovannelli 1947; Heyvaerts et al. 1977; Syrovatskii 1981; Low & Wolfson 1988; Aly & Amari 1997). Magnetic topology analyses of active regions have played a crucial role in understanding the magnetic reconnection processes in 3D in confined flares (see review by Démoulin 2007). In 2D configuration, the reconnection can occur at null points, where the magnetic field vanishes. In 3D, the reconnection can also occur at a null point (Masson et al. 2009), but also along a separator (*e.g.*, Longcope

2005; Parnell et al. 2010a) or a quasi-separatrix layer (QSL, see e.g., Démoulin et al. 1997; Titov et al. 2002; Aulanier et al. 2005; Parlat & Démoulin 2012).

Some atypical flares share several elements common to both the classical definition of eruptive and confined categories, in particular the existence of two parallel ribbons and several other remote ribbons. To the authors' knowledge, three different origins are known for these complex events which, depending on each case, either belong to the eruptive or confined flares category. Firstly, they can be due to a failed filament eruption. The confinement of the filament by coronal arcades eventually makes it stall in the low corona, and eventually reconnect with its restraining arcades (e.g., Török & Kliem 2005; Guo et al. 2010; Chen et al. 2013). Secondly, they can develop when long-distance loop-loop interactions and reconnections are driven by a successful eruption that pushes these loops against their neighbors (e.g., Maia et al. 2003; Chandra et al. 2009). Thirdly, they can appear when two filaments of opposite helicities reconnect with one another without merging (Deng et al. 2002; Schmieder et al. 2004; DeVore et al. 2005; Török et al. 2011; Chandra et al. 2011).

Because of their complexity, many atypical flares have not been analyzed in great details. One could wonder if the usual tools and models that have been developed throughout the years are really relevant for all of these complex events. The question is more preoccupying than it sounds a priori, since these complex under-looked flares may be the most numerous, among all the flares that the Sun produces. We note that the recent paper by Liu et al. (2014) was the first topological study that started addressing this question. Combining a careful EUV analysis with the QSL method, the authors were able to identify their event as being a confined flare associated with a failed flux rope eruption. The aim of our paper is to present and analyze a different but complex event that involved filaments, therefore using the standard flare model and the QSL method. Our single event was merely selected because it was observed with two independent ground based telescopes, namely THEMIS in Tenerife and ARIES in India. It was a C3.3 class flare, that occurred on Oct 16, 2012 in the active region NOAA 11589. This region comprised two filaments, that gradually formed and converged, but did not merge.

The QSL method was first proposed in Démoulin et al. (1997). It is based on the calculation of the photospheric footprints of QSLs, from extrapolated magnetic fields. QSLs are defined as the narrow volumes within which the magnetic field connectivity has very sharp gradients (Priest & Démoulin 1995). They are the 3D generalization of separatrices in 2.5D X-points with an additional guide field (those were called flipping layers by Priest & Forbes 1992). QSLs are preferential sites for the build-up of electric currents and the development of magnetic reconnection in general 3D systems. Among many developments, QSLs have been shown to play an essential role not only in confined flares, but also in eruptive flares (Démoulin et al. 1996; Savcheva et al. 2012; Janvier et al. 2013), possibly in SEP transport towards Earth (Masson et al. 2012) as well as in twisted flux tubes interacting in solar observations (Chandra et al. 2011), in numerical simulations (Milano et al. 1999; Wilmot-Smith et al. 2010; Török et al. 2011) and in laboratory experiments (Lawrence & Gekelman 2009; Gekelman et al. 2012). More details can be found in the reviews by Démoulin (2006) and Aulanier (2011). So as to conduct the QSL method (i.e., to plot the photospheric footprints of QSLs), either the norm  $N$  of the QSL (Démoulin et al. 1997) or its squashing degree  $Q$  (Titov et al. 2002), have to be calculated

at the boundary of the extrapolated fields. Since both  $N$  and  $Q$  provide a different measure for the gradients of the field line connectivity across QSLs, their footprints naturally arise as narrow and elongated layers where  $N$  or  $Q \gg 1$ . In this paper, we apply the QSL method to NOAA 11589, by computing the squashing degree,  $Q$ , at the photospheric level.

The paper is organized as follows. Section 2 presents the observations, with an analysis of the evolution of two filaments in the active region, and the development of the flare. The QSL method and the potential role of QSLs in the flare are discussed in Section 3. In Section 4, we present our interpretation of our results, with an observational evidence for the trigger of the flare, and with a conjecture on the sequences of reconnections in the calculated QSLs that can account for the complex development of the observed atypical flare. Finally, in Section 5, we conclude on the important role of the QSL method in unveiling the sequence of events that shape complex and atypical flares, even when they do not fit the standard model.

## 2. Observations

### 2.1. Data

Part of the observations of NOAA 11589 presented here was obtained with the Atmospheric Imaging Assembly imager (AIA; Lemen et al. 2012) and the Helioseismic and Magnetic Imager (HMI; Schou et al. 2012) onboard the Solar Dynamic Observatory (SDO; Pesnell et al. 2012) satellite. The AIA instrument observes the Sun over a wide range of temperatures from the photosphere to the corona. The pixel size of the AIA images is  $0.6''$ . In this study, we considered the 1600, 304, 193, and 171 Å data. The magnetic field in the AR was studied by using the line-of-sight magnetograms of the HMI instrument which observes the full disk with a pixel size of  $0.5''$ .

We also used ground-based observations of the AR obtained with the indian telescope from the Aryabhata Research Institute of observational Sciences (ARIES), and with the french Téléscope Héliographique pour l'Etude du Magnétisme et des Instabilités Solaires (THEMIS). The 15-cm f/15 Coudé telescope of the ARIES, operating in Nainital (India), observes in the  $H\alpha$  line with a spatial-resolution of  $0.58''$ . The THEMIS telescope, operating in Tenerife (Canary Islands), allows to simultaneously map the  $H\alpha$  emission and the full Stokes parameters in the Fe 6302.5 Å of a field-of-view of about  $240'' \times 100''$  in one hour.

### 2.2. Evolution of the photospheric magnetic field

The AR NOAA 11589 appeared at the heliographic coordinates N13 E61 on 2012 October 10. The AR appeared as two large-scale, decaying magnetic polarities. It presented a  $\beta$  magnetic configuration which evolved towards a  $\beta\gamma\delta$  configuration on October 16. During its on-disk passage, the AR produced 20 C-class flares.

The evolution of the AR during its on-disk passage presented localized magnetic flux emergence episodes together with large-scale magnetic flux cancellation as displayed in Figure 1 (top row). The episodic emerging flux events occurred within the north of the central part of the AR. The violet arrows in Figure 1 highlight two of these emerging flux events which occurred on October 13 and 14.

The magnetograms evolution also presents traces of large-scale magnetic flux cancellation. In particular, we can see that the positive polarity, pointed by the violet arrow in the magnetogram of October 13, was progressively cancelled out. On Oc-

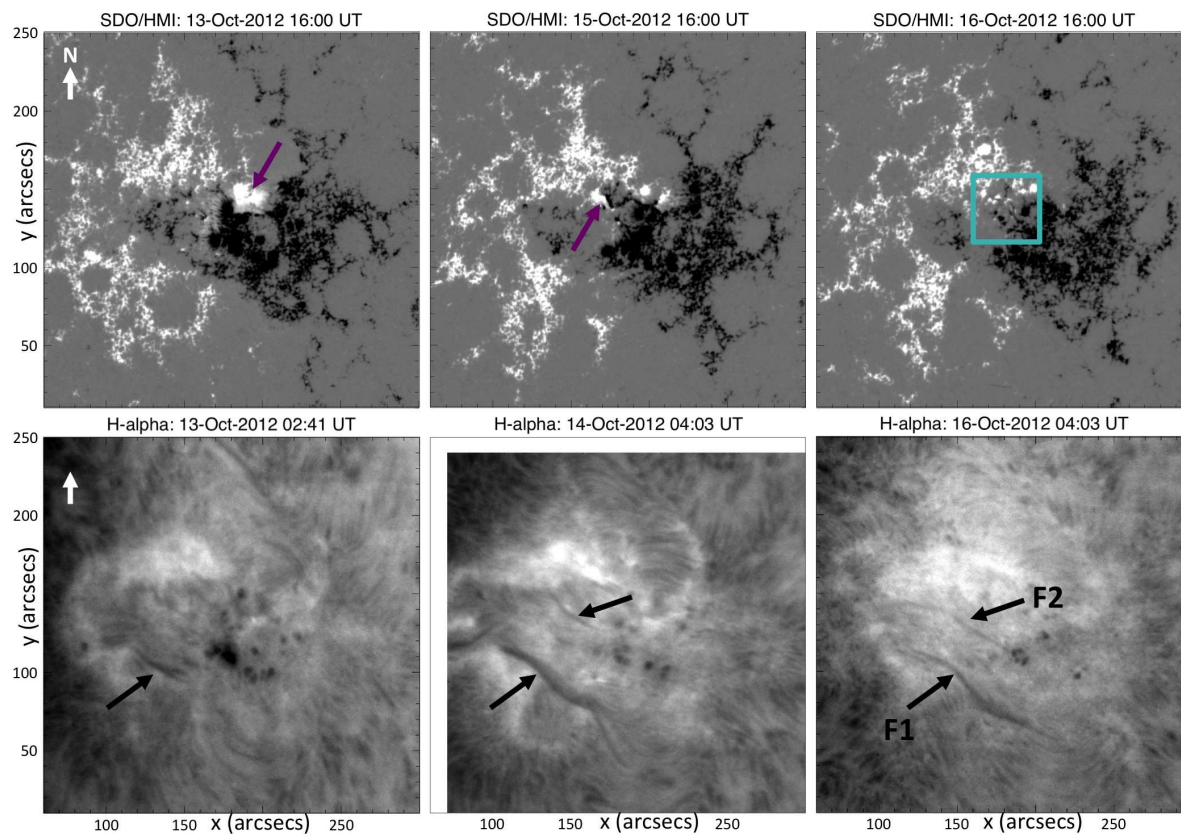


**Fig. 1.** Evolution of active region NOAA 11589 during its disk passage before the eruption on 2012 October 16. Top: Evolution of the longitudinal magnetic field observed by SDO/HMI. White/black are positive/negative polarities. The field strength is saturated at 500 Gauss. The violet arrows indicate significant emerging fluxes on October 13 and 15. The cyan rectangle highlights the region where recurring magnetic flux emergence occurred on October 16 and likely triggered the studied C3-class flare (see Section 2.4). The temporal evolution of the magnetograms is available as a movie in the online edition. Bottom: Development of filaments in  $H\alpha$  observed by ARIES telescope. The locations of two observed filaments F1 and F2 are indicated by black arrows. The white arrow indicates the north direction.

tober 16, this positive polarity had almost vanished. The large-scale flux cancellation is also particularly well observable in the central part of the AR, on the east part of the negative polarity. Indeed, it shows that the easternmost part of the negative polarity moved towards the east and progressively cancelled out with the positive polarity.

### 2.3. Evolution of the two active region filaments

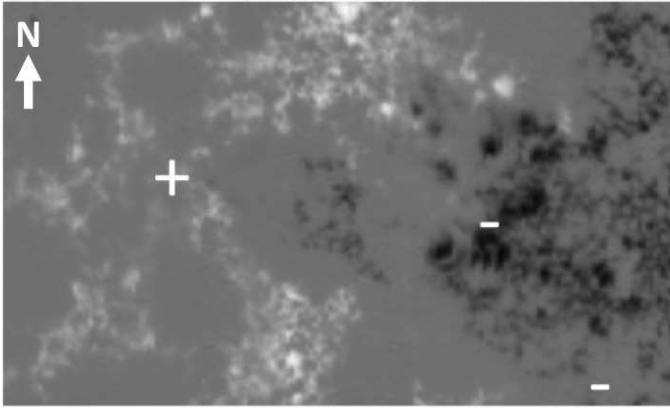
The large-scale magnetic flux cancellation observed in the central part of the AR led to the formation of two filaments (*e.g.*, van Ballegoijen & Martens 1989; Antiochos et al. 1994; Martens & Zwaan 2001; Wang & Muglach 2007). The evolution of these filaments in  $H\alpha$  is presented in Figure 1 (bottom row). The formation of the first filament started on October 13 (see Figure 1). The filament appeared on the southern part of the AR, and progressively evolved towards the thick and elongated filament labeled F1 in the  $H\alpha$  image of Figure 1. The second filament appeared on October 14 in the center of the AR, and progressively evolved towards the filament labeled F2.

Using the  $H\alpha$  data from THEMIS (Figure 2), we were able to derive the chirality of the filaments based on Aulanier & Démoulin (1998) and Mackay et al. (2010). In Figure 2, one of the barbs of filament F1, highlighted by the southern white arrow, indicates that the filament was dextral. In addition, the filament F1 had its easternmost end rooted in the positive polarity and its westernmost end rooted in the negative polarity. This indicates that its axial field was pointing towards

the south-west. Regarding the position of the positive polarity compared with the negative polarity in this region (Figure 1), it follows that the filament was dextral and thus had a negative helicity, which agrees with the orientation of the filament barbs. We note that the filament F1 thus obeyed the hemispheric chirality rule, according to which most of the filaments of the northern hemisphere have a dextral chirality (*e.g.*, Pevtsov et al. 2003). Based on the same analysis, we found that the chirality of filament F2 was sinistral. The filament F2 thus had a positive helicity. Hence, F2 did not obey the hemispheric chirality rule. We thus conclude that NOAA 11589 possessed a mixed magnetic helicity, with positive magnetic helicity in its northern part, and negative magnetic helicity in its southern part (see also Section 3.1).

The evolution of these two filaments shows that the northern footpoints of both filaments converged towards each other without merging. This is in agreement with previous numerical simulation (*e.g.*, DeVore et al. 2005; Aulanier et al. 2006a) and observational studies (*e.g.*, Martin 1998; Schmieder et al. 2004; Chandra et al. 2010; Török et al. 2011; Chandra et al. 2011) showing that the merging of two filaments strongly depends on their chirality and their relative orientation. In particular, the presented filaments evolution would be equivalent to *Experiment 2* of DeVore et al. (2005, see their Fig. 8). Thus, the filaments did not have the opportunity of merging probably because their axial field was oriented in opposite direction along the PIL.

(a) THEMIS/MTR, magnetogram, 2012/10/16



(b) THEMIS/MTR, H $\alpha$ , 2012/10/16

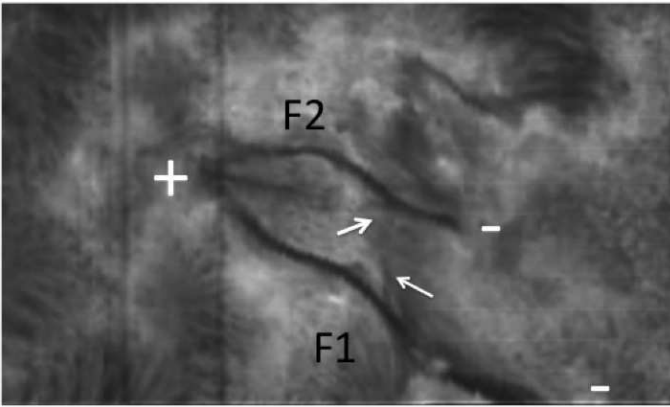


**Fig. 2.** Active region NOAA 11589 observed on 2012 October 16 by THEMIS/MTR between 08:02 and 09:02 UT. Top: Longitudinal magnetic field. Bottom: H $\alpha$  map showing the two recently formed filaments of Figure 1. The white arrows indicate the barbs used to infer the filaments chirality. Filament F1 is a dextral filament, F2 is a sinistral filament. The + and - signs indicate the magnetic field polarity of each end of the filaments. The field of view covers  $\sim 175'' \times 100''$ . The white arrow indicates the north direction.

#### 2.4. The 2012 October 16 flare

On 2012 October 16, the AR was located at heliographic coordinates N13 W11. On that day, the AR produced a C3.3/1F class flare. According to the GOES instruments, the flare started around 16:12 UT, peaked at 16:27 UT, and ended around 16:39 UT. The flare signatures were visible in the different wavelengths observed by the SDO. The 94 Å data from the SDO/AIA indicates that the flare was initiated in the northern part of the AR where magnetic flux emergence was often detected (see the violet arrows in Figure 1).

Figure 3 displays the flare signatures at 1600 and 304 Å during the maximum phase of the flare. These signatures present a similar morphology in both wavelengths. During the flare evolution, the data show the beginning of small, localized brightenings appearing on the north, east, and south parts of the AR. The eastern brightening, which was also the most distinguishable, progressively enhanced and expanded towards the west direction. It formed within the positive polarity, and eventually developed into the eastern ribbon of Figure 3. The northern brightening, which was the less distinguishable, expanded in both the east and west directions. It developed into the northern ribbon of Figure 3 which formed within the positive polarity. This northern ribbon

expanded and eventually merged with the eastern ribbon, forming a single, extended ribbon within the positive polarity of the AR. The southern brightening, which formed within the negative polarity, expanded towards the north-west direction, forming the extended southern ribbon. Overall, the observations show that the flare-ribbons developed into two single, extended ribbons that formed around both filaments, one ribbon within the positive polarity, the other within the negative polarity. We note that such ribbons are compatible with the two typical flare-ribbons associated with the classical eruptive and confined flares involving the presence of a filament. Finally, the observations indicate that, at the extended southern ribbon, another brightening developed towards the south-west direction between 16:14 and 16:39 UT. This brightening was probably related to plasma ejection.

Figure 4 presents the evolution of the flare signatures during the decay phase at 193 Å. In this figure, we clearly see the formation of post-flare loops joining the two extended flare-ribbons displayed in Figure 3. From the AR evolution at 193 and 171 Å, we found that the first post-flare loops developed in the northern part of the AR. One of these northern post-flare loops is labeled  $L_1$  in Figure 4. This post-flare loop was quickly followed by the formation of post-flare loops  $L_2$  and  $L_3$  within the central part of the AR. These post-flare loops were then followed by the formation of  $L_4$ , and a bulk of post-flare loops in the central part of the AR.

According to the CSHKP model, both eruptive and confined flares — involving the presence of a filament — should be associated with the formation of hot post-flare loops *below* the erupting filament, whether its eruption succeeds or fails (see also Schmieder et al. 1995, 1996; Shibata & Magara 2011; Aulanier et al. 2012). Interestingly, we find that the post-flare loops formed *above* the filaments. Furthermore, the observations indicates that none of the two filaments seemed to be neither disturbed nor erupting during or after the flare. These two features are not consistent with any standard model of eruptive or confined flare. It follows that the two extended flare-ribbons associated with the flare can neither be explained by a successful, nor a failed, filament eruption. A topological analysis is then required to build-up a plausible flare scenario that explains the observed flare dynamics and its associated signatures.

### 3. Magnetic topology of the active region

#### 3.1. Magnetic field extrapolation

The topological analysis of AR 11589 magnetic field requires the knowledge of the magnetic field in the coronal volume containing the AR. In practice, the coronal magnetic field can be estimated from linear (*e.g.*, Nakagawa & Raadu 1972; Alissandrakis 1981; Démoulin et al. 1989) or nonlinear (see reviews by Wiegmann & Sakurai 2012; Régner 2013, and references therein) force-free field extrapolations (LFFF or NLFFF), defined by

$$\nabla \times \mathbf{B} = \alpha \mathbf{B}, \quad (1)$$

using photospheric data as a bottom boundary condition. In Equation (1), the force-free parameter,  $\alpha$ , is uniform in space for LFFF extrapolations, and is constant along each elemental flux tubes for NLFFF extrapolations.

Recent studies have shown that NLFFF extrapolations are becoming more and more reliable for inferring the coronal magnetic field from photospheric vector magnetograms (*e.g.*, Schrijver et al. 2008; Canou & Amari 2010; Valori et al. 2012;

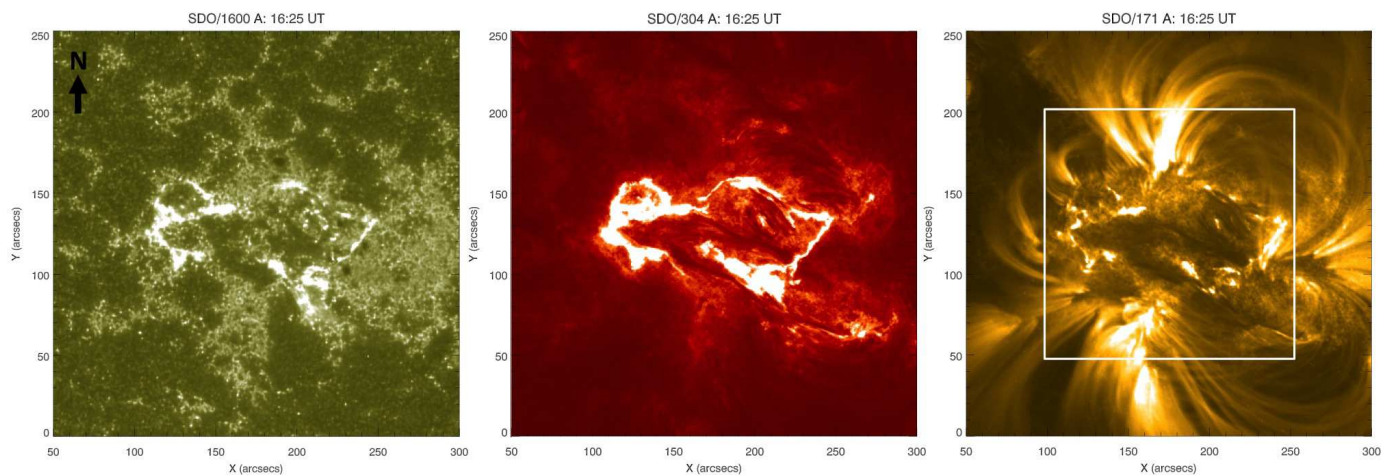


**Fig. 3.** Flare signatures observed by SDO/AIA on 2012 October 16, at 1600 Å (left), at 304 Å (middle), and at 171 Å (right). The black arrow indicates the north direction. The white square indicates the field-of-view of Figure 4. The temporal evolution of AIA 1600 Å, 304 Å, and 171 Å images is available as a movie in the online edition.

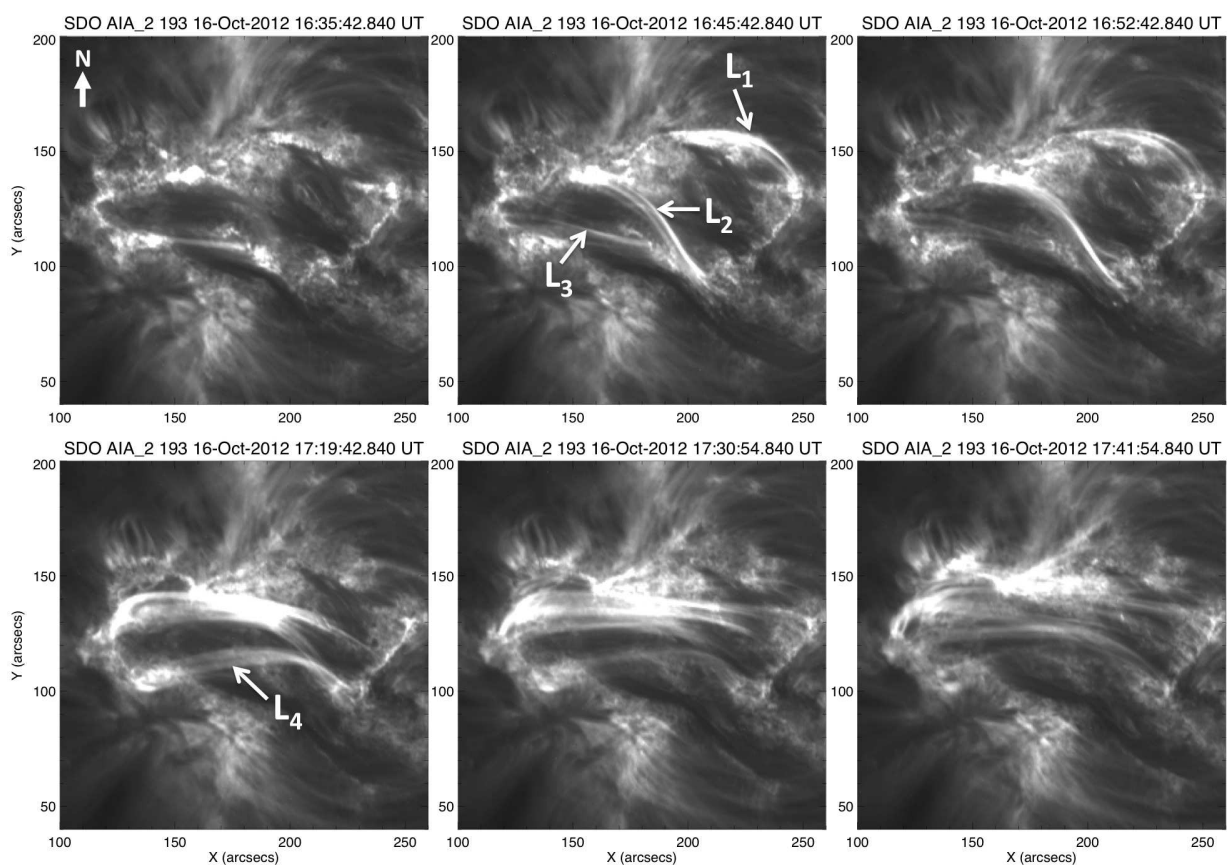


**Fig. 4.** Flare signatures observed by SDO/AIA on 2012 October 16 at 193 Å. On the top-left panel, the white arrow indicates the north direction.

Wiegmann et al. 2012; Guo et al. 2012; Jiang & Feng 2013). Because the EUV data show that AR 11589 was formed of filaments of opposite chirality (see Figure 2) and loops of opposite  $\alpha$ -values (see Equation (1)), one may want to consider NLFFF extrapolations to study the topology of the AR.

However, there are two reasons for not considering such extrapolation models in the present study. First, the filaments were located in the plage regions, hence, where the magnetic field is weak and the photospheric electric currents, and local  $\alpha$ -values, are not well measured. This would tend to give a nearly po-

tential magnetic field within these regions, which would prevent from retrieving the filaments in an NLFFF extrapolation (e.g., McClymont et al. 1997; Leka & Skumanich 1999; Wiegmann 2004). The second reason is given by the EUV data showing that none of the filaments seemed to be affected by the evolution of the flare. Indeed, both filaments were still present with the same shape before and after the flare. In addition, the EUV data show that the post-flare loops were formed *above* the filaments contrary to what is expected from the CSHKP model (see Section 2.4). Together, these observations *a priori* suggest that the

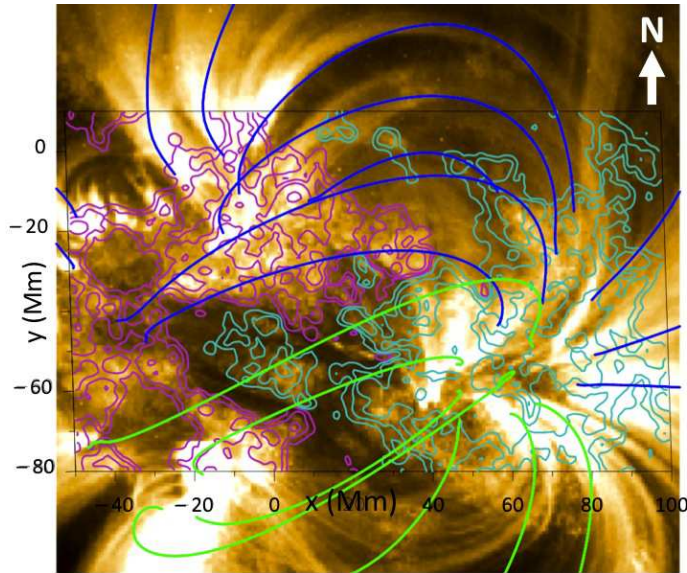


**Fig. 5.** Zoom on NOAA 11589 at 15:00 UT on 2012 October 16, observed with SDO/AIA at 171 Å and overplotted with selected magnetic field lines from the extrapolation ( $\alpha = 7 \times 10^{-3} \text{ Mm}^{-1}$ ). Blue/green lines are magnetic field lines which give a good/poor match with the AR’s coronal loops. Solid purple/cyan lines display isocontours of the photospheric magnetic field,  $B_z = [30, 100, 300, 1000]$  Gauss. The white arrow indicates the north direction.

flare mechanism only involved the magnetic field surrounding the filaments, and not the magnetic field of the filaments. It is therefore possible to focus the topological analysis of AR 11589 on its global magnetic field using simple LFFF extrapolations.

We thus used Equation (1) with a spatially uniform  $\alpha$  to perform a set of LFFF extrapolations. The extrapolations were achieved using the method described in Alissandrakis (1981) for 5 distinct LFFF, such that  $\alpha = [-7, -3.5, 0, 3.5, 7] \times 10^{-3} \text{ Mm}^{-1}$ . The method uses fast Fourier transform (FFT) to solve the Helmholtz’s equation for a LFF magnetic field of force-free parameter  $\alpha$ . The four side boundary conditions are therefore periodic. There is no top boundary condition because the unphysical eigenmodes that increase with height are discarded. The magnetogram used as the bottom boundary condition ( $z = 0$ ) for the extrapolation covers a domain of  $368 \times 255 \text{ Mm}^2$  and was taken at 15:00 UT, *e.g.*, about one hour before the beginning of the flare. Due to the fact that the magnetic field evolves only weakly during several days, the exact choice of the magnetogram is not determining.

The extrapolations were performed using a  $xy$ -domain roughly twice larger in each direction — padded with zeros — in order to limit aliasing effects. We extrapolated the magnetic field up to  $z = 2000 \text{ Mm}$ , leading to an extrapolation domain covering  $700^2 \times 2000 \text{ Mm}^3$  on a non-uniform grid containing  $1024^2 \times 351$  points. Within the set of performed extrapolations, we kept the extrapolation giving the best match with the northern loops of the AR because this is the region where the flare was initiated according to the SDO/AIA 94 Å data. Using the metrics introduced in Green et al. (2002), we found that the force-free parameter for this extrapolation is  $\alpha = 7 \times 10^{-3} \text{ Mm}^{-1}$ . Figure 5 displays selected field lines of the magnetic field of this extrapolation in the central part of the AR, plotted over the SDO/AIA 171 Å data.

## 3.2. QSLs in the active region

### 3.2.1. QSLs and flare-ribbons

The computation of the squashing degree,  $Q$ , in the extrapolation domain was performed using method 3 ofariat & Démoulin (2012). Figure 6a displays the photospheric mapping of QSLs by showing  $\log Q$  at  $z = 0$ . Plotting magnetic field lines over the  $\log Q$  map, we identified three QSLs connected to each other (see Figure 6). The value of  $Q$  in these QSLs is typically about  $10^3 - 10^4$  which is indicative of strong connectivity gradients. For clarity, these three QSLs are highlighted and labeled  $Q_i$  ( $i = \{1, 2, 3\}$ ) in Figure 6b. They are respectively compared with the three identified ribbon-systems,  $R_i$ , in Figure 6c.

At this point, it must be re-emphasized that QSLs depend on the magnetic field connectivity (*e.g.*, Démoulin et al. 1996), which depends on the extrapolation assumptions. This means that extrapolations with different assumptions may lead to different QSLs. In some cases, these QSLs could even disappear. For consistency, we thus reconsidered all the other extrapolations performed, *i.e.*,  $\alpha = [-7, -3.5, 0, 3.5] \times 10^{-3} \text{ Mm}^{-1}$ , and we computed the squashing degree for all of them (see Figure 7).

The photospheric footprints of QSLs together with magnetic field lines plotting revealed that these three QSLs are reliable (see Figures 7 and 8). Indeed, they are present in each considered LFFF extrapolations with similar shapes and locations, meaning that they are topologically robust structures. There are only few differences that lie on the shapes and intersections of the QSLs footprints. In particular, Figures 7 and 8 show that while  $Q_2$  and  $Q_3$  are always connected regardless of the value of the force-free parameter,  $Q_1$  and  $Q_2$  are solely connected when the force-free parameter of the LFFF extrapolation is positive or null. From the photospheric mapping of  $Q$  (see Figure 7), it is clear that only LFFF extrapolations with a positive (or null) force-free parameter display QSLs footprints which have a morphology that is compatible with the flare-ribbons shown Figures 3 and 6. These two figures further justify the use of a positive force-free parameter to analyze the topology of the AR’s magnetic field, and our choice to consider the extrapolation giving the best match with the northern coronal loops where  $Q_1$  and the trigger of the flare were located. Among our LFFF extrapolations, we found that the QSLs from the  $\alpha = 7 \times 10^{-3} \text{ Mm}^{-1}$  extrapolation give the best match with the flare-ribbons shape (see Figure 6c). We emphasize that a magnetic field extrapolation performed about 30 minutes after the flare, using  $\alpha = 7 \times 10^{-3} \text{ Mm}^{-1}$ , further shows that the three identified QSLs were also temporally robust because they subsisted throughout the duration of the flare (see panels (a) and (c) of Figures 7 and 8).

Together with magnetic field lines plotting, Figure 6a allows to distinguish between two double C-shaped QSL footprints,  $Q_{\{1,2\}}$ , and a circular-like QSL,  $Q_3$ , in agreement with the three flare-ribbons,  $R_i$  (see also Figure 8a). A few discrepancies are found between the QSLs footprints and the flare-ribbons shape and location, which results in a rather poor overlay (not shown here). We found the main discrepancies in the identification of  $Q_{3,curv}$ , and in the relative positions of  $Q_2$  and  $R_2$ . The first is related to the difficulty of distinguishing  $R_{3,curv}$  from  $R_{1,arc}$  and  $R_{2,curv}$  in the AIA 1600 Å images while it is possible in the extrapolation. The observations tend to suggest that, in the real configuration,  $Q_{1,arc}$ ,  $Q_{2,curv}$  and  $Q_{3,curv}$  are more entangled than in the extrapolation. The second is related to the deformation of  $R_{2,arc}$  compared with  $Q_{2,arc}$ , and the displacement of  $R_{2,curv}$  compared with  $Q_{2,curv}$ . The extrapolation shows that  $Q_{2,arc}$  is much closer to the PIL than suggested by the corresponding

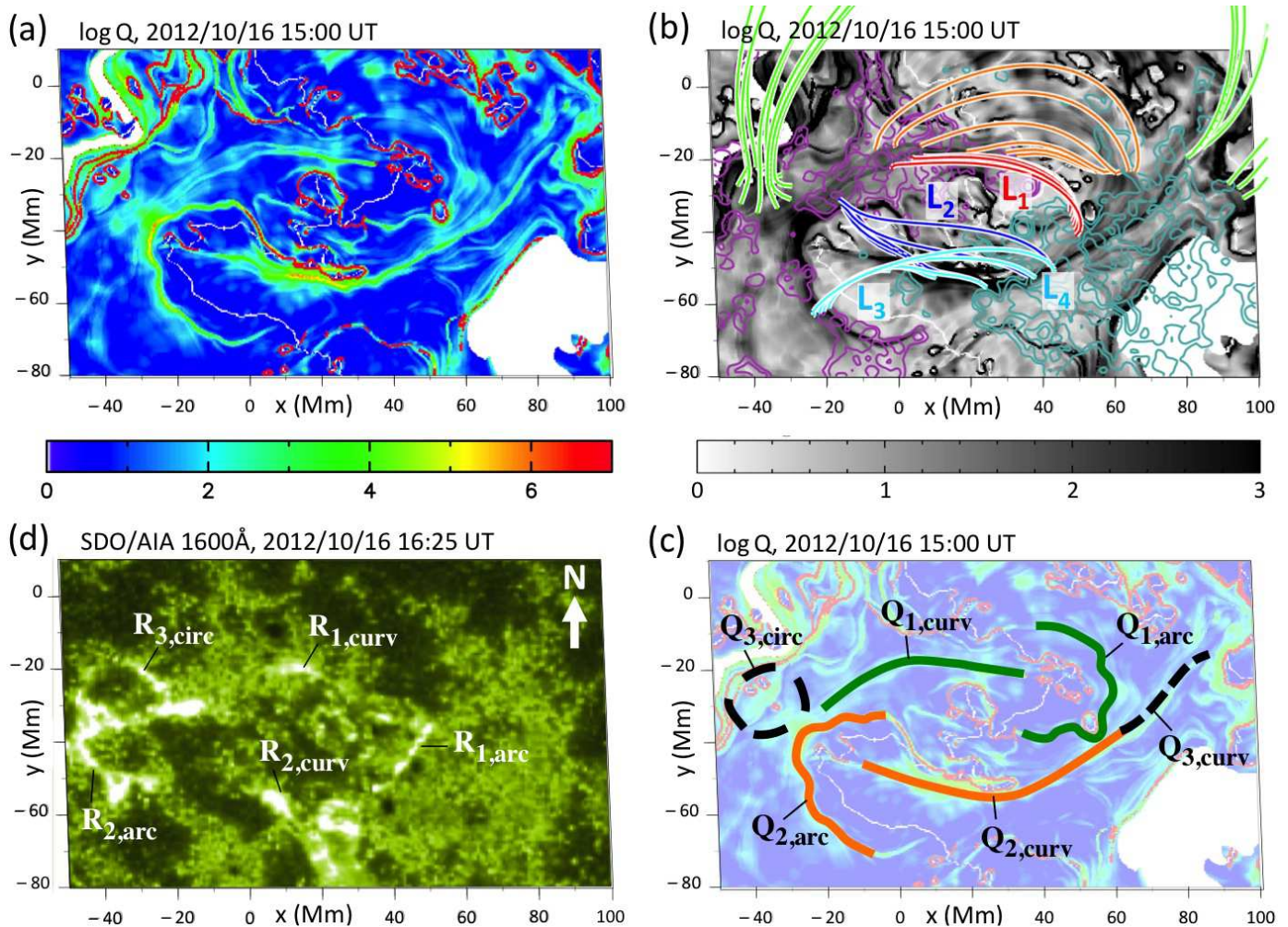


**Fig. 6.** Zoom on NOAA 11589. (a) Photospheric mapping of QSLs from the computation of the squashing degree,  $Q$ . White regions are related to magnetic field lines which are open at the scale of the extrapolation domain, and where  $Q$  is not computed. (b) Selected magnetic field lines and (c) photospheric footprints of the identified QSLs plotted over the photospheric  $Q$ -map. The field-lines labeled  $L_{i=(1,2,3,4)}$  indicate possible candidates for the four post-flare loops labeled in Figure 4. (d) Flare-ribbons labelled with respect to the identified QSLs footprints. The white arrow indicates the north direction.

flare-ribbon. Also,  $Q_{2,curv}$  is very close to the PIL of the northern filament while the associated ribbon locates it more in the central part between the two filaments.

It is arguable that all these discrepancies are related to the assumption we made by only considering the global magnetic field of the AR and extrapolating it in LFFF. Indeed, such a hypothesis does not allow to model the highly-stressed filament magnetic fields and their close surroundings. This probably results in local modifications of the connectivity of magnetic field lines, which are responsible for the deformation and displacement of the QSLs in our extrapolation, as compared with the shape and location of the flare-ribbons. Nevertheless, distinctive discrepancies between QSLs footprints and flare-ribbons can also be found in NLFFF extrapolations. Indeed, this clearly appears in the atypical flare studied by Liu et al. (2014), as can be seen in their Figures 7(d) and 7(e). We thus conjecture that such mismatches between QSLs footprints and flare-ribbons are more generally inherent to the force-free model of choice.

Despite the aforementioned discrepancies, we find a good qualitative agreement between the QSLs footprints and the flare ribbons of our studied event. This match validates the use of a simplified LFFF model to study the topology of AR 11589 and relate it to the origin of the flare.

Finally, Figure 6a further exhibits two types of very-high  $Q$ -regions: the long red stripes closed to the open-field regions (white areas in the  $Q$ -map) at the East/West edges of the AR, and the red segments and round-shapes. The first are due to the aliasing from the periodic boundary conditions and are spurious. The second are due to very low-altitude null-points located above small parasitic polarities. These small QSLs may sustain magnetic reconnection, and lead to small-scale jets and bright-points. However, they are unrelated to the flare because their field lines do not intersect the QSL system  $Q_{1,2,3}$ . We therefore ignore them in our analysis.

### 3.2.2. A complex interlinked topology

Figure 6b displays a cartoon of the inferred magnetic topology plotted over the photospheric  $Q$ -map. It comprises the two double C-shaped QSLs (green and orange QSLs) that resemble the QSL of the quadrupolar magnetic configuration from Titov et al. (2002) or Aulanier et al. (2005). The cartoon also shows that the green and orange QSLs are connected to each other via a third QSL whose footprints have a shape very similar to the QSL of the null-point configuration studied in Masson et al. (2009) and Reid et al. (2012).

While we did not find a null-point associated with  $Q_3$ , the topology of the magnetic field in the region of  $Q_{3,circ}$ , as well as the corresponding circular flare-ribbons, are typical signatures of the presence of a magnetic null-point (see *e.g.*, Masson et al. 2009; Wang & Liu 2012; Deng et al. 2013). The circular-like shape of the positive magnetic polarity in this region and the low negative magnetic flux suggest the presence of a very low-lying, nearly photospheric null-point. The absence of a null-point in the corresponding region of our LFFF extrapolation is very likely related to the strength of the magnetic field measured by HMI. Indeed, in the region of  $Q_3$ , the HMI data display three distinctive negative magnetic polarities whose magnetic field is of the order of  $\lesssim 9$  Gauss, which is lower than the 10 Gauss of HMI sensitivity. We conjecture that the absence of a null-point in the corresponding region of our LFFF extrapolation is not inherent to the extrapolation, but is due to a poor precision in the measurement of the weak negative flux — whose strength is comparable to the instrument sensitivity — which prevents from retrieving the null.

Overall, the above results show that AR 11589 presents a complex topology which comprises two double C-shaped QSLs, one quasi-separator that links them both (Parnell et al. 2010a), and a possible null-point. Such a topology is favorable for the build-up of electric current layers at any of the identified QSLs (*e.g.*, Aulanier et al. 2005; Haynes et al. 2007). Furthermore, any disturbance of any of these topological systems is likely to trigger magnetic reconnection at all the others (*e.g.*, Parnell et al. 2008, 2010b).

## 4. A confined flare above filaments

### 4.1. Driver

To identify the possible driver of the observed C3.3 flare, we considered HMI and AIA 1600 Å data sets at a 12-min cadence within a range of 4 hours prior to, and after, the flare.

Before the flare, the region of the magnetogram enclosed by the cyan rectangle in Figure 9a displayed spatially-aperiodic successions of opposite magnetic polarities in directions oriented from the north-east towards the south-west. These patterns were spatially correlated with Ellerman bombs (EBs; Ellerman 1917) as highlighted in Figure 9c. EBs are small recurring brightenings often observed in the photospheric wings of chromospheric lines (*e.g.*, Vorpahl & Pope 1972; Kurokawa et al. 1982; Qiu et al. 2000; Georgoulis et al. 2002; Bernasconi et al. 2002; Pariat et al. 2004, 2007; Fang et al. 2006; Bello González et al. 2013; Vissers et al. 2013). They are believed to be the result of bald-patch reconnection occurring along undulatory, or serpentine, flux tubes as they cross the photosphere and emerge into the solar corona (see Pariat et al. 2004; Cheung et al. 2010). Our LFFF extrapolation suggests that such serpentine flux tubes were indeed present prior to the flare, in the region hosting EBs, as shown Figure 9d. Finally, Figure 9b shows that a new bipole appeared some time after the flare, as inferred from the broad patches of opposite polarities present in the center of the cyan rectangle and which are accompanied with small-scale bipolar patches.

Such observational features are clear signatures of magnetic flux emergence starting hours before the flare onset. This emergence occurred below the QSL  $Q_1$ , in between the western part of the  $Q_{1,curv}$  and the southern part of the  $Q_{1,arc}$  branches. Furthermore, this region below  $Q_1$  corresponds to the location of the first flare brightennings. So this continuous emergence below  $Q_1$  may well have induced magnetic reconnection at this

QSL. It may thus have been responsible for the trigger of the flare (*e.g.*, Schmieder et al. 1997; Bagalá et al. 2000; del Zanna et al. 2006). Hence, we conjecture that continuous emergence starting prior to the flare, and occurring below the northern QSL of the AR, was the driver of the observed C-class flare.

### 4.2. Proposed flare scenario

We propose that the observed C-class flare was the result of a multiple-step reconnection mechanism driven by magnetic flux emergence below  $Q_1$ . In this scenario, the continuous magnetic flux emergence below  $Q_1$  leads to the accumulation of magnetic stress at  $Q_1$ , which results in the build-up of an electric current layer at this QSL (*e.g.*, Milano et al. 1999; Aulanier et al. 2005; Török et al. 2009). This emergence leads to the intensification and the thinning of this current layer, which eventually triggers slipping/slip-running magnetic reconnection (Aulanier et al. 2006b), at  $Q_1$ , of the emerging field with the ambient pre-existing magnetic field.

Because of the proximity of  $Q_{1,arc}$  with  $Q_{2,curv}$  and  $Q_{3,curv}$ , or  $Q_{1,curv}$  with  $Q_{2,arc}$  and  $Q_{3,circ}$ , the slipping/slip-running magnetic reconnection at  $Q_1$  is likely to stress the magnetic field of  $Q_2$  and  $Q_3$  since magnetic stress can be transported at all QSLs via the quasi-separator that links the QSLs all together (*e.g.*, Priest & Titov 1996; Galsgaard & Nordlund 1997; Parnell et al. 2008). Indeed, at the quasi-separator, the QSLs share common magnetic field lines. The stress of such field lines at one of the QSLs is thus likely to also build-up stress at the quasi-separator and/or at the other QSL(s) sharing these field lines. Such a stress may build-up electric currents at  $Q_2$  and  $Q_3$ , or may increase pre-existing electric currents within these two QSLs. Eventually, the induced stress of  $Q_2$  and/or  $Q_3$  triggers magnetic reconnection at these two QSLs.

In our scenario, the flare is thus the consequence of continuous slow emergence of magnetic flux below  $Q_1$ , which results in slipping/slip-running reconnection at this QSL, eventually triggering reconnection at the two other interlinked QSLs. Particle acceleration is thus expected at all QSLs, implying the formation of flare-ribbons at all QSLs footprints, and post-flare loops anchored into the flare-ribbons (*e.g.*, Gorbachev & Somov 1989; Schmieder et al. 1997; Mandrini et al. 2006; Baker et al. 2009; Chandra et al. 2011), as supported by the AIA 1600 and 193 Å data in Figures 6 and 4 in this particular event.

It must be emphasized that all three QSLs involved in our flare scenario are located above the two observed non-eruptive filaments which are passive during the flare that spreads in the corona *above* and *around* them. This *a posteriori* supports the assumption made in Section 3.1, that the flare mechanism did not involve the magnetic field of the filaments. Our scenario thus explains the formation of the two extended flare-ribbons around the two filaments, as the consequence of sequential magnetic reconnection occurring in a complex system of three interlinked QSLs located above the filaments.

## 5. Summary and Discussion

In this study, we used multi-wavelength, high-resolution observations obtained by the SDO, ARIES and THEMIS instruments, so to analyze the dynamics of the magnetic field of AR NOAA 11589 that led to a non-standard C3.3 class flare on 2012 October 16. The AR evolution was associated with large-scale magnetic flux cancellation that led to the formation of two filaments of opposite chirality. Unlike what the standard model

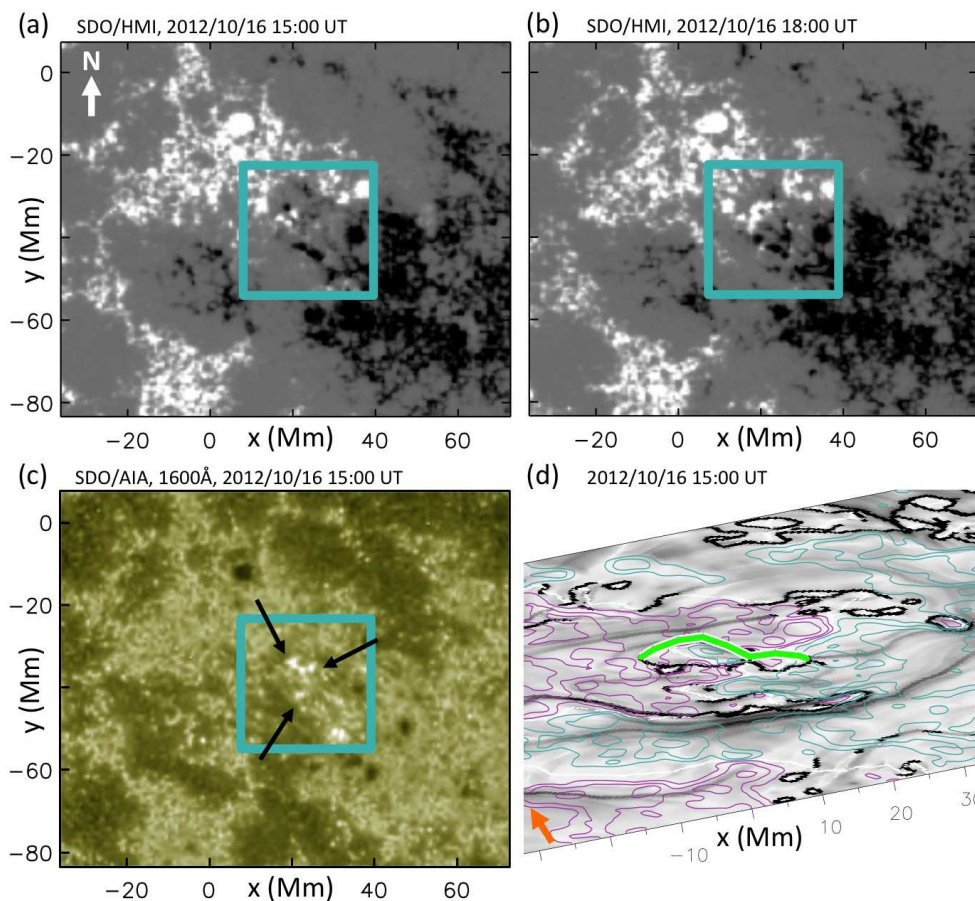


**Fig. 9.** Signatures of magnetic flux emergence occurring in NOAA 11589 around the time of the flare. The cyan rectangle highlights the region of magnetic flux emergence. HMI magnetograms in greyscale (a) before the flare, and (b) after the flare. The temporal evolution of the magnetograms is available as a movie in the online edition. (c) AIA 1600 Å image showing some EBs which are highlighted by the black arrows. (d) extrapolated serpentine field line (green) associated with the EBs shown panel (c), plotted over the photospheric mapping of the QSLs (greyscale). Solid purple/cyan lines show the same  $B_z$  isocontours as in Figure 5. The white and orange arrows indicate the north direction.

predicts, the flare loops formed *above* and not *below* the filaments. Furthermore, the latter were apparently *not* involved in the flare mechanism, since they did not erupt. The dataset considered here also presented the signatures of localized magnetic flux emergence episodes in the northern part of the AR. Our analysis indicates that the flare was driven by one of these episodes that actually took place below a complex system of quasi-separatrix layers (QSLs), as calculated in a linear force-free field (LFFF) extrapolation. This continuous magnetic flux emergence presumably stressed the magnetic field of the QSLs, thus resulting in the development of narrow and intense current layers within them. This scenario implies the occurrence of multiple and sequential magnetic reconnections within the complex set of QSLs, which led to the observed flare. This scenario is supported by the relatively good match found between the expected timing of the QSL activations, the shape of the QSL footprints, and the development and morphology of complex flare ribbons and loops as observed in the EUV (see online movies associated with Figures 3 and 4).

By performing a set of LFFF extrapolations using different values of the force-free parameter, we have demonstrated the robustness of the derived complex topology, and hence of our results. More generally, our study shows the stability of the QSLs related to large-scale coronal loops/magnetic fields that are not associated with a magnetic flux-ropes. In particular, it shows the stability of such QSLs (1) against changes — within a certain range — of the force-free parameter for LFFF extrapolations (see also Aulanier et al. 2005), and (2) against temporal variations that do not result in a major evolution of the photospheric magnetic flux and/or of electric currents (see also the large-scale QSL of the quadrupolar AR 11158 in Zhao et al. 2014). We re-

call that the force-free parameter controls the amount of electric current density in magnetic field lines, which can be observationally related to the photospheric transverse/horizontal magnetic field. Therefore, the stability of the QSLs of large-scale coronal loops/magnetic fields — that are not associated with a magnetic flux-ropes — suggests that such QSLs are mainly constrained by the photospheric longitudinal/vertical magnetic field, hence, by the large-scale distribution of the photospheric magnetic flux.

It is worth noticing that the flare scenario that we proposed is based on one important conjecture, namely that slip-running reconnection may activate several QSLs which are linked together. This may be expected because reconnecting field lines may slip from one QSL to another. In this picture, a given field line may reconnect at least two times in the considered magnetic configuration. Such sequences of magnetic reconnections for a given field line have already been reported for magnetic configurations with separatrices intersecting at a separator (*e.g.*, Galsgaard & Nordlund 1997; Haynes et al. 2007; Parnell et al. 2010a). However, to the authors' knowledge, it has never been shown to occur in complex QSL systems in which two QSLs are located in the vicinity of one another. Therefore, this conjecture should be addressed by future numerical experiments in which the initial magnetic field configurations should possess two neighboring QSLs.

The C3.3 class flare analyzed in this paper is a typical example of an atypical flare exhibiting signatures common to both standard and confined solar flares. Indeed, at large scales, the flare initially appears to be associated with the formation of two extended ribbons that developed parallel to and aside the filaments, in a globally bipolar active region, just like in the standard model. However, at smaller scales, the polarity inversion line is

strongly curved. The ribbons have a complex shape, and they did not brighten simultaneously. Together, these two features suggest some coupling of remote regions that did not seem to be magnetically linked to the filaments. Furthermore, the filaments did neither erupt, nor were they associated with any failed eruption. Explaining this type of atypical events in general may be a challenge for the usual eruptive and confined flare models. Nevertheless, the topological analysis of the magnetic field derived from a force-free extrapolation, here achieved using the QSL method (applied with the squashing degree,  $Q$ ; Démoulin et al. 1997), shows that it is possible to explain atypical flare signatures as a complex QSL system which allows to couple remote regions via slip-running reconnection (Aulanier et al. 2006b).

On the one hand, this work further confirms that QSLs play a key role for 3D reconnection in solar flares, as reported in previous studies of less complex events (*e.g.*, Schmieder et al. 1997; Mandrini et al. 2006; Chandra et al. 2011). On the other hand, this study suggests that topological analyses, such as the QSL method (using either  $N$  or  $Q$ ), may also be the answer to explaining atypical solar flares, that may actually be more numerous than the more classical eruptive and confined flares which are often analyzed in the literature. This conclusion is further confirmed by the topological analysis of a different atypical flare studied, in the framework of the QSL method, by Liu et al. (2014). In their event, the magnetic configuration was derived using a nonlinear force-free field (NLFFF) extrapolation. Similarly to our event, the derived configuration possessed a large-scale QSL above a magnetic flux-rope (although our event was associated with two QSLs and two filaments, each QSL lying above a filament). As in our case, the flare was likely driven by magnetic flux emergence occurring below the large-scale QSL, in a region different from the flux-rope location, and which eventually triggered magnetic reconnection at this QSL. However, contrary to our event, the continuous reconnection at the large-scale QSL of their configuration eventually destabilized the flux-rope whose eruption failed due to the presence of strong confining arcades above it.

If atypical solar flares are the most numerous, then the study by Liu et al. (2014) and ours suggest that the classical paradigm of confined and eruptive flares should be revisited. Note, however, that these are only two independent case studies, so further topological analyses of atypical solar flares, either using LFFF or NLFFF extrapolations, are required to confirm such a statement and that topological studies are indeed relevant for all these complex events.

*Acknowledgements.* We thank the referee for helpful comments that improved the paper. We deeply thank Dr. W. Uddin for providing us with the observations of the ARIES telescope. We thank all the team of THEMIS for adjusting the telescope during our observing campaign and the director, Bernard Gelly for providing us with the data. K.D. thanks E. Pariat for fruitful discussions that helped in identifying the driver of the flare. R.C. thanks the Observatoire de Paris for the grant given during his stay in Meudon in January 2013. We acknowledge the open data policy of NASA/SDO.

## References

Alissandrakis, C. E. 1981, *A&A*, 100, 197  
 Aly, J. J. & Amari, T. 1997, *A&A*, 319, 699  
 Antiochos, S. K., Dahlburg, R. B., & Klimchuk, J. A. 1994, *ApJ*, 420, L41  
 Aulanier, G. 2011, in *IAU Symposium*, Vol. 273, *IAU Symposium*, ed. D. Prasad Choudhary & K. G. Strassmeier, 233–241  
 Aulanier, G. & Démoulin, P. 1998, *A&A*, 329, 1125  
 Aulanier, G., DeVore, C. R., & Antiochos, S. K. 2006a, *ApJ*, 646, 1349  
 Aulanier, G., Janvier, M., & Schmieder, B. 2012, *A&A*, 543, A110  
 Aulanier, G., Pariat, E., & Démoulin, P. 2005, *A&A*, 444, 961

Aulanier, G., Pariat, E., Démoulin, P., & DeVore, C. R. 2006b, *Sol. Phys.*, 238, 347  
 Bagalá, L. G., Mandrini, C. H., Rovira, M. G., & Démoulin, P. 2000, *A&A*, 363, 779  
 Baker, D., van Driel-Gesztelyi, L., Mandrini, C. H., Démoulin, P., & Murray, M. J. 2009, *ApJ*, 705, 926  
 Bello González, N., Danilovic, S., & Kneer, F. 2013, *A&A*, 557, A102  
 Bernasconi, P. N., Rust, D. M., Georgoulis, M. K., & Labonte, B. J. 2002, *Sol. Phys.*, 209, 119  
 Canou, A. & Amari, T. 2010, *ApJ*, 715, 1566  
 Carmichael, H. 1964, *NASA Special Publication*, 50, 451  
 Chandra, R., Jain, R., Uddin, W., et al. 2006, *Sol. Phys.*, 239, 239  
 Chandra, R., Pariat, E., Schmieder, B., Mandrini, C. H., & Uddin, W. 2010, *Sol. Phys.*, 261, 127  
 Chandra, R., Schmieder, B., Aulanier, G., & Malherbe, J. M. 2009, *Sol. Phys.*, 258, 53  
 Chandra, R., Schmieder, B., Mandrini, C. H., et al. 2011, *Sol. Phys.*, 269, 83  
 Chen, H., Ma, S., & Zhang, J. 2013, *ApJ*, 778, 70  
 Cheung, M. C. M., Rempel, M., Title, A. M., & Schüssler, M. 2010, *ApJ*, 720, 233  
 del Zanna, G., Berlicki, A., Schmieder, B., & Mason, H. E. 2006, *Sol. Phys.*, 234, 95  
 Démoulin, P. 2006, *Adv. Space Res.*, 37, 1269  
 Démoulin, P. 2007, *Advances in Space Research*, 39, 1367  
 Démoulin, P., Bagala, L. G., Mandrini, C. H., Henoux, J. C., & Rovira, M. G. 1997, *A&A*, 325, 305  
 Démoulin, P., Priest, E. R., & Anzer, U. 1989, *A&A*, 221, 326  
 Démoulin, P., Priest, E. R., & Lonie, D. P. 1996, *J. Geophys. Res.*, 101, 7631  
 Deng, N., Tritschler, A., Jing, J., et al. 2013, *ApJ*, 769, 112  
 Deng, Y., Lin, Y., Schmieder, B., & Engvold, O. 2002, *Sol. Phys.*, 209, 153  
 DeVore, C. R., Antiochos, S. K., & Aulanier, G. 2005, *ApJ*, 629, 1122  
 Ellerman, F. 1917, *ApJ*, 46, 298  
 Fang, C., Tang, Y. H., Xu, Z., Ding, M. D., & Chen, P. F. 2006, *ApJ*, 643, 1325  
 Forbes, T. G. & Malherbe, J. M. 1986, *ApJ*, 302, L67  
 Galsgaard, K. & Nordlund, Å. 1997, *J. Geophys. Res.*, 102, 231  
 Gekelman, W., Lawrence, E., & Van Compernelle, B. 2012, *ApJ*, 753, 131  
 Georgoulis, M. K., Rust, D. M., Bernasconi, P. N., & Schmieder, B. 2002, *ApJ*, 575, 506  
 Giovanelli, R. G. 1947, *MNRAS*, 107, 338  
 Gorbachev, V. S. & Somov, B. V. 1989, *Soviet Ast.*, 33, 57  
 Green, L. M., López fuentes, M. C., Mandrini, C. H., et al. 2002, *Sol. Phys.*, 208, 43  
 Guo, Y., Ding, M. D., Liu, Y., et al. 2012, *ApJ*, 760, 47  
 Guo, Y., Ding, M. D., Schmieder, B., et al. 2010, *ApJ*, 725, L38  
 Hanaoka, Y. 1997, *Sol. Phys.*, 173, 319  
 Haynes, A. L., Parnell, C. E., Galsgaard, K., & Priest, E. R. 2007, *Royal Society of London Proceedings Series A*, 463, 1097  
 Heyvaerts, J., Priest, E. R., & Rust, D. M. 1977, *ApJ*, 216, 123  
 Hirayama, T. 1974, *Sol. Phys.*, 34, 323  
 Janvier, M., Aulanier, G., Pariat, E., & Démoulin, P. 2013, *A&A*, 555, A77  
 Jiang, C. & Feng, X. 2013, *ApJ*, 769, 144  
 Kopp, R. A. & Pneuman, G. W. 1976, *Sol. Phys.*, 50, 85  
 Kurokawa, H., Kawaguchi, I., Funakoshi, Y., & Nakai, Y. 1982, *Sol. Phys.*, 79, 77  
 Kusano, K., Bamba, Y., Yamamoto, T. T., et al. 2012, *ApJ*, 760, 31  
 Lawrence, E. E. & Gekelman, W. 2009, *Physical Review Letters*, 103, 105002  
 Leka, K. D. & Skumanich, A. 1999, *Sol. Phys.*, 188, 3  
 Lemen, J. R., Title, A. M., Akin, D. J., et al. 2012, *Sol. Phys.*, 275, 17  
 Liu, R., Titov, V. S., Gou, T., et al. 2014, *ApJ*, 790, 8  
 Longcope, D. W. 2005, *Living Reviews in Solar Physics*, 2, 7  
 Low, B. C. & Wolfson, R. 1988, *ApJ*, 324, 574  
 Mackay, D. H., Karpen, J. T., Ballester, J. L., Schmieder, B., & Aulanier, G. 2010, *Space Sci. Rev.*, 151, 333  
 Maia, D., Aulanier, G., Wang, S. J., et al. 2003, *A&A*, 405, 313  
 Mandrini, C. H., Démoulin, P., Bagala, L. G., et al. 1997, *Sol. Phys.*, 174, 229  
 Mandrini, C. H., Démoulin, P., Schmieder, B., et al. 2006, *Sol. Phys.*, 238, 293  
 Martens, P. C. & Zwaan, C. 2001, *ApJ*, 558, 872  
 Martin, S. F. 1998, *Sol. Phys.*, 182, 107  
 Masson, S., Aulanier, G., Pariat, E., & Klein, K.-L. 2012, *Sol. Phys.*, 276, 199  
 Masson, S., Pariat, E., Aulanier, G., & Schrijver, C. J. 2009, *ApJ*, 700, 559  
 McClymont, A. N., Jiao, L., & Mikic, Z. 1997, *Sol. Phys.*, 174, 191  
 Milano, L. J., Dmitruk, P., Mandrini, C. H., Gómez, D. O., & Démoulin, P. 1999, *ApJ*, 521, 889  
 Moore, R. L., Sterling, A. C., Hudson, H. S., & Lemen, J. R. 2001, *ApJ*, 552, 833  
 Nakagawa, Y. & Raadu, M. A. 1972, *Sol. Phys.*, 25, 127  
 Nishio, M., Yaji, K., Kosugi, T., Nakajima, H., & Sakurai, T. 1997, *ApJ*, 489, 976  
 Pariat, E., Aulanier, G., Schmieder, B., et al. 2004, *ApJ*, 614, 1099  
 Pariat, E. & Démoulin, P. 2012, *A&A*, 541, A78

- Pariat, E., Schmieder, B., Berlicki, A., et al. 2007, *A&A*, 473, 279
- Parnell, C. E., Haynes, A. L., & Galsgaard, K. 2008, *ApJ*, 675, 1656
- Parnell, C. E., Haynes, A. L., & Galsgaard, K. 2010a, *Journal of Geophysical Research (Space Physics)*, 115, 2102
- Parnell, C. E., Maclean, R. C., & Haynes, A. L. 2010b, *ApJ*, 725, L214
- Pesnell, W. D., Thompson, B. J., & Chamberlin, P. C. 2012, *Sol. Phys.*, 275, 3
- Pevtsov, A. A., Balasubramaniam, K. S., & Rogers, J. W. 2003, *ApJ*, 595, 500
- Priest, E. R. & Démoulin, P. 1995, *J. Geophys. Res.*, 100, 23443
- Priest, E. R. & Forbes, T. G. 1992, *J. Geophys. Res.*, 97, 1521
- Priest, E. R. & Forbes, T. G. 2002, *A&A Rev.*, 10, 313
- Priest, E. R. & Titov, V. S. 1996, *Royal Society of London Philosophical Transactions Series A*, 354, 2951
- Qiu, J., Ding, M. D., Wang, H., Denker, C., & Goode, P. R. 2000, *ApJ*, 544, L157
- Régnier, S. 2013, *ArXiv e-prints*
- Reid, H. A. S., Vilmer, N., Aulanier, G., & Pariat, E. 2012, *A&A*, 547, A52
- Savcheva, A., Pariat, E., van Ballegoijen, A., Aulanier, G., & DeLuca, E. 2012, *ApJ*, 750, 15
- Schmieder, B., Aulanier, G., Demoulin, P., et al. 1997, *A&A*, 325, 1213
- Schmieder, B., Heinzel, P., van Driel-Gesztelyi, L., & Lemen, J. R. 1996, *Sol. Phys.*, 165, 303
- Schmieder, B., Heinzel, P., Wiik, J. E., et al. 1995, *Sol. Phys.*, 156, 337
- Schmieder, B., Mein, N., Deng, Y., et al. 2004, *Sol. Phys.*, 223, 119
- Schou, J., Borrero, J. M., Norton, A. A., et al. 2012, *Sol. Phys.*, 275, 327
- Schrijver, C. J., De Rosa, M. L., Metcalf, T., et al. 2008, *ApJ*, 675, 1637
- Shibata, K. 1999, *Ap&SS*, 264, 129
- Shibata, K. & Magara, T. 2011, *Living Reviews in Solar Physics*, 8, 6
- Shibata, K., Masuda, S., Shimojo, M., et al. 1995, *ApJ*, 451, L83
- Sturrock, P. A. 1966, *Nature*, 211, 695
- Syrovatskii, S. I. 1981, *ARA&A*, 19, 163
- Titov, V. S., Hornig, G., & Démoulin, P. 2002, *J. Geophys. Res.*, 107, 1164
- Török, T., Aulanier, G., Schmieder, B., Reeves, K. K., & Golub, L. 2009, *ApJ*, 704, 485
- Török, T., Chandra, R., Pariat, E., et al. 2011, *ApJ*, 728, 65
- Török, T. & Kliem, B. 2005, *ApJ*, 630, L97
- Valori, G., Green, L. M., Démoulin, P., et al. 2012, *Sol. Phys.*, 278, 73
- van Ballegoijen, A. A. & Martens, P. C. H. 1989, *ApJ*, 343, 971
- Vissers, G. J. M., Rouppe van der Voort, L. H. M., & Rutten, R. J. 2013, *ApJ*, 774, 32
- Vorpahl, J. & Pope, T. 1972, *Sol. Phys.*, 25, 347
- Wang, H. & Liu, C. 2012, *ApJ*, 760, 101
- Wang, Y.-M. & Muglach, K. 2007, *ApJ*, 666, 1284
- Wiegelmann, T. 2004, *Sol. Phys.*, 219, 87
- Wiegelmann, T. & Sakurai, T. 2012, *Living Reviews in Solar Physics*, 9, 5
- Wiegelmann, T., Thalmann, J. K., Inhester, B., et al. 2012, *Sol. Phys.*, 281, 37
- Wilmot-Smith, A. L., Pontin, D. I., & Hornig, G. 2010, *A&A*, 516, A5
- Zhao, J., Li, H., Pariat, E., et al. 2014, *ApJ*, 787, 88

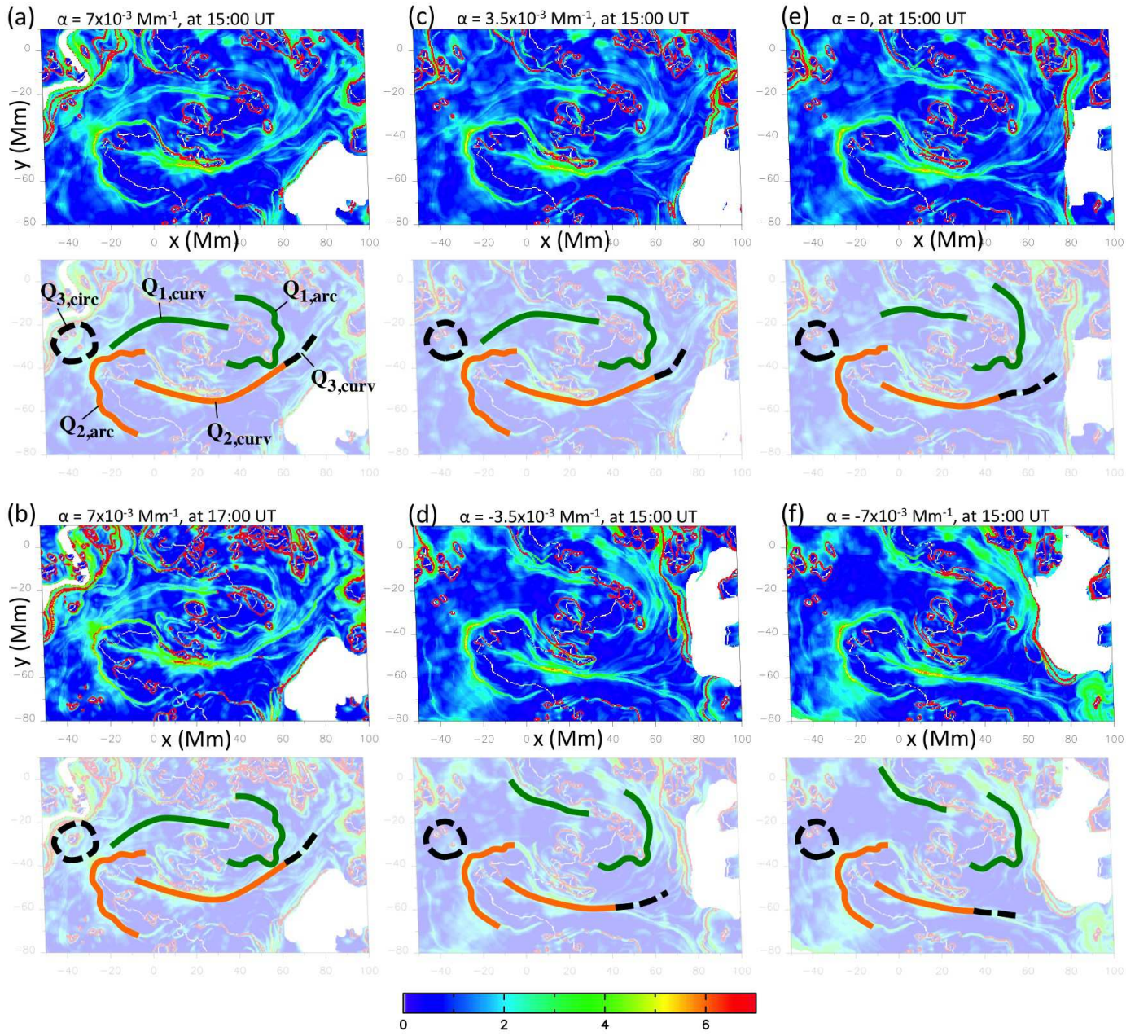


**Fig. 7.** Photospheric mapping of the QSLs of NOAA 11589, from the computation of the squashing degree,  $Q$ , for all our LFFF extrapolations. (a, c, e, d, f)  $\sim 1$  hour before the flare, at 15:00 UT for  $\alpha = [7, 3.5, 0, -3.5, -7] \times 10^{-3} \text{ Mm}^{-1}$ . (b)  $\sim 30$  minutes after the flare, at 17:00 UT, for  $\alpha = 7 \times 10^{-3} \text{ Mm}^{-1}$  (*i.e.*, the value considered in this paper).

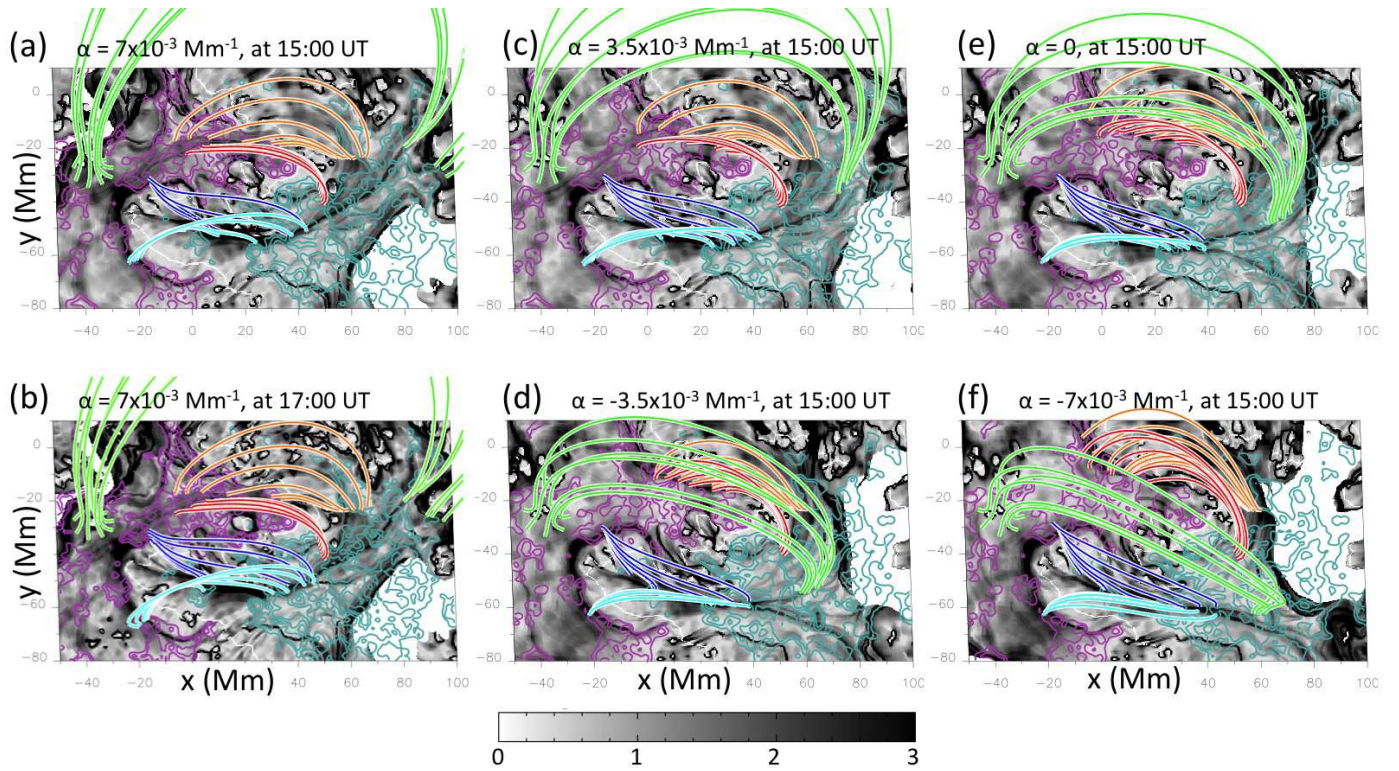


**Fig. 8.** Selected field lines belonging to the three QSLs of NOAA 11589 identified in Figure 6b, for the same extrapolations as in Figure 7. Red/orange, dark/light-blue, and green field lines respectively belong to  $Q_1$ ,  $Q_2$ , and  $Q_3$ . The grey-scale displays the photospheric map of the squashing degree,  $Q$ . Solid purple/cyan lines are isocontours of the photospheric vertical magnetic field,  $B_z = [150, 300, 600]$  Gauss.